Experimental and Theoretical NANOTECHNOLOGY
http://etn.siats.co.uk/

Phase transition of InN films via trimethylindium flows

A. Hanson[1,*], *A. Motengen*[2]

[1]University of Gothenburg, Department of Physics, SE-405 30 Gothenburg, Sweden
[2]University of Oslo, Department of Physics, 0316 Oslo, Norway
*Email: hansoa@gu.se

Received: 7/2/2020 / *Accepted:* 5/7/2020 / *Published:* 1/9/2020

Wurtzite (*w*) and zincblende (*zb*) InN films have been grown on (011) $\mathrm{SrTiO_3}$ (STO) substrates by metal- organic chemical vapor deposition, the epitaxial relation- ships and optical properties are characterized by X-ray diffraction (XRD), absorption and photoluminescence (PL). Based on XRD θ–2θ and Φ scanning results, the epi- taxial relationships between (*w*- and *zb*-) InN films and STO substrates are determined, that is, $(0001)[11\underline{2}0]_{w\text{-InN}}(011)[100]_{\text{STO}}$ and $(100)[011]_{zb\text{-InN}}//(011)[100]_{\text{STO}}$. Compared with the *w*-InN films, the *zb*-InN films exhibit a red shift in absorption edge and PL spectra, and a much nar- rower and stronger PL spectrum, implying a better optical quality of *zb*-InN films. The structure transition is supposed to be due to the difference in atom and bond areal density between the crystal plane of *w*-InN(0001) and *zb*-InN(100).

Keywords: InN; Nanostructure; Phase tranition.

1. INTRODUCTION

The group-III nitrides provide enormous potential applications in optoelectronics, because they cover the entire visible and near-ultraviolet spectrum. Amongst them, InN films have attracted much attention in terms of its narrow band gap and a high mobility [1, 2]. Up to now, a huge majority of research on InN has been concentrated on the hexagonal wurtzite form, which is the thermodynamic stable phase at usual growth conditions. Nevertheless, zincblende InN (*zb*-InN) with a cubic symmetry is also interesting because it is predicted to possess superior electronic properties for de- vice applications [3–7]. For instance, the cubic structure can improve the device performances due to the isotropic nature of properties and absent/reduced built-in spontaneous polarization. Furthermore, it is expected to have a lower band-gap energy than wurtzite InN (*w*-InN), which would expand the application of group-III nitrides more toward the infrared region. Since the lattice of zincblende structure is isotropic, the phonon scattering would be lower and *zb*-InN is expected to have a higher saturated electron drift velocity than *w*-InN. Also, since both *n*- and *p*-type doping are known to be most efficient in zincblende structure III–V semiconductors, cubic InN is expected to be easier to dope than wurtzite. The metastable *zb*-InN phase have been obtained on cu- bic substrates (In_2O_3, YSZ and MgO) [3–5], nitrided or indium pre-deposited sapphire substrates [6, 7]. However, as far as we know, little is reported to realize *zb*-InN on $SrTiO_3$ (STO), which is often used as a substrate to deposit functional oxide films. If high-quality *zb*-InN films can be grown on STO substrates, multifunctional devices integrating the superior optoelectronic properties of *zb*-InN with the rich functional characters of perovskites could be developed in the future. In this paper, we obtained *zb*-InN on (011) STO substrates using metal-organic chemical vapor deposition (MOCVD) by decreasing the flow rate of indium precursor.

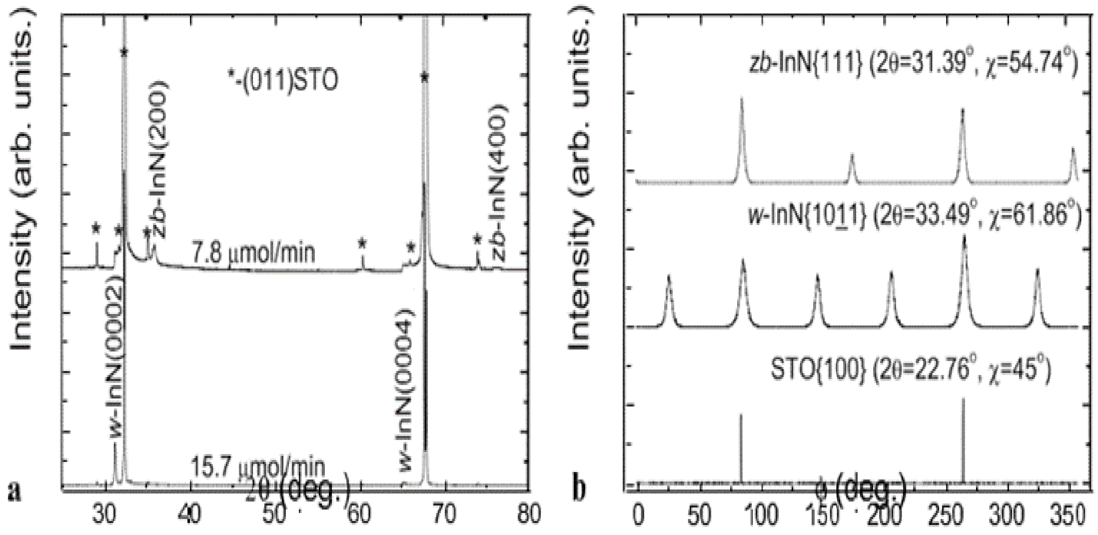

Figure 1 (a) XRD (b) Scanning patterns.

2. EXPERIMENTS

InN films were grown on (011) STO single crystal sub- strates in a horizontal MOCVD reactor. The substrates were sequentially cleaned with organic solvents and rinsed with de-ionized water. InN films were grown by utilizing trimethylindium (TMIn) and ammonia (NH_3) as precursors. The utilized growth parameters were as follows: TMIn, 7.8 and 15.7 micromoles/minute (μmol/min); NH_3, 3 standard liter per minute; V/III ratio, ~17000 and 8500; pressure, 760 Torr; temperature, 580°C; time, 30 minutes (min). The surface and cross-sectional morphologies were character- ized by field-emission scanning electron microscope (SEM) (Hitachi, S4800). The epitaxial relationships are determined by X-ray θ–2θ (Panalytical, X'Pert Pro MPD) and Φ scan- ning (Rigaku, TTR III) patterns with Cu-Kα radiation. The infrared absorption spectra were taken in range of 5000–15000 cm^{-1} with a resolution of

4 cm^{-1} at room temper- ature (Bruker, IFS120HR). Photoluminescence (PL) spec- tra were performed using a Fourier transform spectrometer equipped with a solid-state laser emitting 532 nm of 100 mW and InGaAs detector at 12 K (Bruker, IFS120HR).

3. RESULTS AND DISCUSSION

Figure 1a shows XRD θ–2θ scanning patterns of InN films deposited on (011) STO substrates under different flow rates of TMIn. InN films exhibit evidently different structures, that is, wurtzite (0002) (*w*-InN) at a TMIn flow rate of 15.7 µmol/min and zincblende (200) (*zb*-InN) at a reduced TMIn flow rate of 7.8 µmol/min. The intensity scale of Fig. 1a is linear, and the curve of 7.8 µmol/min is enlarged by several times for clarity, so that the small signals of *zb*-InN can be seen clearly, but little *w*-InN is seen from this curve, therefore the 7.8 µm/min sample seems to be somewhat pure *zb*-InN from Fig. 1a. From the XRD peak position shown in Fig. 1a, the lattice constants for *w*- and *zb*-InN can be calculated to be $c_{w\text{-InN}}$ = 5.7034 Å and $a_{zb\text{-InN}}$ = 4.9914 Å, respectively, which are larger than those of bulk *w*- and *zb*- InN, that is, $c_{w\text{-InN}}$ = 5.669 Å [8] and $a_{zb\text{-InN}}$ = 4.932 Å [9]. The out-of-plane residual strain. X-ray Φ scans are performed to identify the in-plane orientation relationships between the films and substrates. In a Φ scan, the number of peaks corresponds to the number of planes for a particular family that possesses the same angle with the crystal surface, while the separation between peaks correlates with the angular separation between the corresponding projections of the normals to the scanning fam- ily onto the crystal surface. In STO single crystal, there are three crystal planes belonging to the {100} family, (100), (010), (001), but only the latter two have the same angle of 45° with the (011) surface plane ((011) STO substrates are used in the present work), while the former one is perpendicular to the (011) surface plane. Generally, the crystal planes, which are neither perpendicular nor parallel to the surface, are used to obtain the Φ scanning patterns. Under the condition of $2\theta = 22.76°$ and $\chi = 45°$, two reflection peaks separated by 180° are shown from STO {100} family, implying {100} family, it is proved that the (011) STO substrates in the present work are cubic single crystal; while from the rel- ative peak positions in the Φ scans of STO {100}, *w*-InN $\{10\underline{1}1\}$ and *zb*-InN {111}, the in-plane epitaxial relationship between InN films and STO substrates can be deter- mined. Similar to the Φ scanning of STO {100} family, the reflections from *w*-InN $\{10\underline{1}1\}$ ($2\theta = 33.49°$, $\chi = 61.86°$), and *zb*-InN {111} ($2\theta = 31.39°$, $\chi = 54.74°$) families show six and four peaks separated by 60° and 90°, respectively, as shown in Fig. 1b, implying a sixfold and fourfold symme- try as expected. The peak positions in the Φ scans of STO {100}, *w*-InN $\{10\underline{1}1\}$ and *zb*-InN {111} coincide, implying that the intersections of scanning family with the sur- face are parallel to each other. Hence the epitaxial relation- ships between *w*-InN, *zb*-InN films and STO substrates are, respectively, $[11\underline{2}0]_{w\text{-InN}}//[100]_{\text{STO}}$, $[1\underline{1}00]_{w\text{-InN}}//[01\underline{1}]_{\text{STO}}$, and $[011]_{zb\text{-InN}}//[100]_{\text{STO}}$, $[01\underline{1}]_{zb\text{-InN}}//[01\underline{1}]_{\text{STO}}$, as shown in Fig. 1c, d. The lattice mismatches along the directions of $[100]_{\text{STO}}$ and $[01\underline{1}]_{\text{STO}}$ are −10.3% and 9.8% for *w*-InN films, −10.7% and 26.3% for *zb*-InN films, respectively. For both *w*- and *zb*-InN films, each of these lattice mismatches will induce a tensile and compressive strain along the di- rection of $[100]_{\text{STO}}$ and $[01\underline{1}]_{\text{STO}}$. According to Poisson's relation, there is an in-plane compressive strain, which will lead to the stretching out of InN films in the growing direc- tion from XRD θ–2θ scanning patterns shown in Fig. 1a. It implies that the lattice mismatch along the direction of $[01\underline{1}]_{\mathrm{STO}}$ plays an more important role in the residual strain in both *w*- and *zb*-InN films than that of $[100]_{\mathrm{STO}}$. Furthermore, the lattice mismatch along the direction of $[01\underline{1}]_{\mathrm{STO}}$ for *zb*-InN films is larger than that of *w*-InN, which is consistent with the larger out-of-plane residual tensile strain in the *zb*-InN films.

It is interesting that the crystal structure of InN films transit from wurtzite to zincblende when decreasing the flow rate of TMIn, although the lattice mismatch between *zb*- InN and STO is larger than that between *w*-InN and STO. The structure transition of III–V thin films has been found to be strongly dependent on growth temperature, pressure, doping, diameter, epitaxial burying, and metal flux [10–15]. The effect of metal flux on structure is considered to be controlled by initial stage nucleation kinetics. Generally, there are three basic steps in MOCVD growth: adsorption of metal organic precursors on the substrate surface, decomposition of the precursors resulting in the deposition of In and N atoms, surface diffusion and incorporation of adatoms at preferred sites [10]. Based on these steps, we suppose that the wurtzite to zincblende transition of InN films is due to different quantities of In (or N) atoms required to form one monolayer. Therefore, it is crucial to compare the atom and bond areal density for crystal planes of *zb*-InN(100) and *w*- InN(0001). As expected, the atom areal density for the crystal plane of *zb*-InN(100) (8.22×10^{14} cm^{-2}) is smaller than that of *w*-InN(0001) (9.42×10^{14} cm^{-2}). To estimate the more important quantity of the bond areal density, we considered the in-plane atomic arrangements at both *w*- and *zb*- InN/STO interfaces.

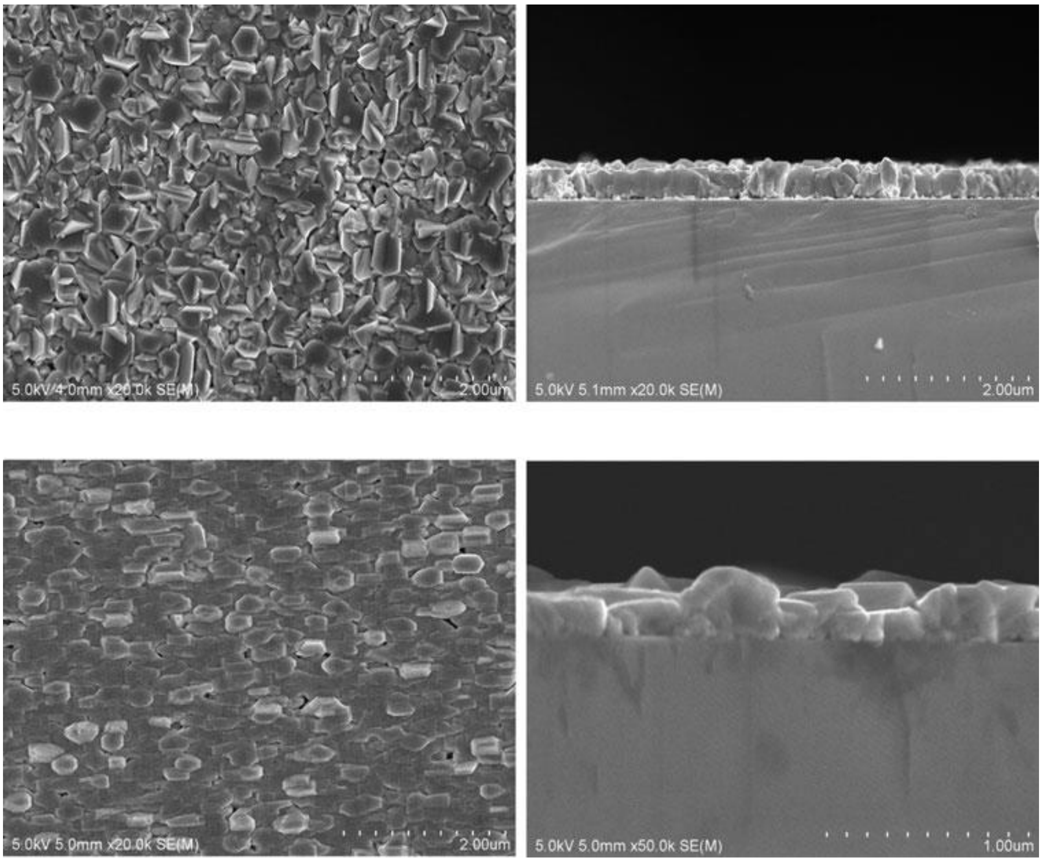

Figure 2 The surface and cross-sectional scanning electron microscopies of w-InN (a, b) and zb-InN (c, d) films on (011) STO substrates. of the (0001)*w*-InN/(011)STO and (100)*zb*-InN/(011)STO interfaces. In these figures, only the N atoms and SrTiO atoms closest to the interface are shown. Due to the large in-plane lattice mismatch between (*w*- and *zb*-) InN and STO, the arrangements of SrTiO-N bonds show the superstructure.

The surface and cross-sectional SEM morphology of *w*- and *zb*-InN films on STO substrates are shown in Fig. 2. A flake-like growth mode is found in the *w*-InN films, which is similar to that of *w*-InN films on (111) STO substrates [16]. However, it turns into a long strip shape in the same direction in *zb*-InN films, in accordance with the rather different lattice mismatch in the two vertical directions of $[100]_{\mathrm{STO}}$ and $[01\underline{1}]_{\mathrm{STO}}$. Both *w*- and *zb*-InN films show microcrystallites with hexagonal shape from Fig. 2, implying that hexagonal grains exist in both films. How- ever, the hexagonal grains are not detected in *zb*-InN films by XRD shown in Fig. 1a because of its limited resolution. This phenomenon has also been observed in (110)ZnO by Wu et al. [17]. The interfaces between InN and STO are quite sharp, and no obvious new phase resulting from chem- ical reaction in the interface is observed. The thickness of *w*-InN films (450 nm) is almost two times of that of *zb*-InN (250 nm), which is consistent with the fact that the TMIn flow rate provided for growing *w*-InN is twice of that for *zb*- InN. The crystalline quality of both *w*- and *zb*-InN films are not too high, see Fig. 2. However, it is meaningful to investigate these samples because some qualitative results can still be concluded from them.

To check the optical qualities of *w*- and *zb*-InN films on STO substrates, we measured the absorption and PL spec- tra by a Fourier transform infrared spectrometer. Figure 3a shows the squared absorption coefficient α^2 of InN films as a function of photon energy. The α^2 first rises gradually and then steeply to about 10^9 cm^{-2} with increasing photon energy, which is the typical absorption intensity for di- rect band-gap semiconductors [18, 19]. The optical band gap is determined to be about 0.96 and 0.87 eV for *w*- and *zb*- InN films by extrapolating the linear part to $\alpha^2 = 0$. The band-gap energy of *w*-InN films is much larger than that of *zb*-InN, which is consistent with Hsiao's results [6]. The Hall mobility and carrier concentration of the *w*- and *zb*- InN layers at room temperature are 136.9 and 64.2 $\mathrm{cm}^2/\mathrm{V\,s}$, 4.2×10^{19} and 7.8×10^{19} cm^{-3} measured by the van der Pauw method. The Hall mobility of *w*-InN films is much larger than that of *zb*-InN, which is possible due to the much thicker and denser morphology of *w*-InN than that of *w*-InN. Compared with the absorption edge of *zb*-InN reported by Hsiao [6], there is a blue shift of 0.25 eV in our *zb*-InN, possibly resulting from the larger carrier den- sity in the present work than that of Hsiao's due to Burstein- Moss shift. From the PL spectra of *w*-InN and *zb*-InN films measured at 12 K and 100 mW, as shown in Fig. 3b, it can be seen that the PL peaks of the *w*- and *zb*-InN films are located at 0.81 and 0.78 eV, respectively. The red shift of *zb*-InN compared with *w*-InN in PL spectra is much smaller than that in absorption edge, which is also observed by Hsiao [6]. Moreover, *zb*-InN films exhibit a much narrower and more than four times stronger PL spectra than *w*-InN, implying a better optical quality of *zb*-InN films. The absorption and PL spectra of InN films depend on the crystal structure, crystal quality and carrier density due to Burstein-Moss effect [6]. So the different band gaps of the two samples should reflect the crystal structure, crystal quality and carrier density. Thus, it is somewhat meaningful to show the optical results of the two samples in the present work.

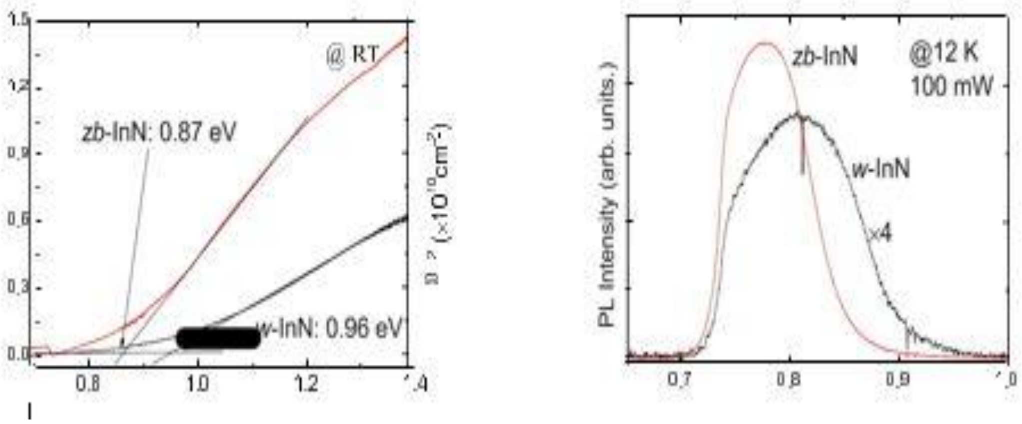

Figure 3 The squared absorption coefficient as a function of photon energy recorded at room temperature and PL spectra measured at 12 K and 100 mW for *w*-InN and *zb*-InN films on (011) STO substrates

4 CONCLUSIONS

In summary, *w*- and *zb*-InN films have been grown on (011) STO substrates by MOCVD. Based on XRD θ–2θ and Φ scanning results, the epitaxial relationships have been determined to be $(0001)[11\bar{2}0]_{w\text{-InN}}//(011)[100]_{\mathrm{STO}}$ and $(100)[011]_{zb\text{-InN}}//(011)[100]_{\mathrm{STO}}$ for *w*- and *zb*-InN, respectively. The *zb*-InN films show a larger out-of-plane residual tensile strain determined by XRD θ–2θ scanning results, which is consistent with the larger in-plane lattice mismatch along $[01\bar{1}]_{\mathrm{STO}}$ for *zb*-InN than that for *w*-InN by XRD Φ scanning results. Flake- and long strip-like surface morphologies have been found for *w*- and *zb*-InN films, re- spectively. Compared with the *w*-InN films, the *zb*-InN films exhibit a red shift in absorption edge and PL spectra, and a much narrower and stronger PL spectra, implying a bet- ter optical quality of *zb*-InN films. The structure transition is supposed to be due to the difference in atom and bond areal density for the crystal plane of *w*-InN(0001) and *zb*- InN(100).

References

[1] M. Losurdo, M.M. Giangregorio, G. Bruno, T.H. Kim, P. Wu, S. Choi, A. Brown, F. Masia, M. Capizzi, A. Polimeni, Appl. Phys. Lett. 90, (2007) 011910
[2] N. Takahashi, A. Niwa, T. Nakamura, J. Phys. Chem. Solids 65 (2004) 1259
[3] J.G. Lozano, F.M. Morales, R. Garcia, D. Gonzalez, V. Lebe- dev, C.Y. Wang, V. Cimalla, O. Aambacher, Appl. Phys. Lett. 90,
(2007) 091901
[4] T. Nakamura, T. Kataoka, R. Katayama, T. Yamamoto, K. Onabe, Phys. Status Solidi 5, (2008) 1712
[5] Y. Iwahashi, H. Yaguchi, A. Nishimoto, M. Orihara, Y. Hijikata, S. Yoshida, Phys. Status Solidi 3, (2006) 1515
[6] C.L. Hsiao, T.W. Liu, C.T. Wu, H.C. Hsu, G.M. Hsu, L.C. Chen, W.Y. Shiao, C.C. Yang, A. Gallstrom, P.P. Holtz, C.C. Chen, K.H. Chen, Appl. Phys. Lett. 92, (2008) 111914
[7] Z.X. Bi, J. Cryst. Growth 300, (2007) 123
[8] S. Chernkov, P. Badov, Experimental and Theoretical NANOTECHNOLOGY 3 (2019) 175
[9] Joint Committee of Powder Diffraction Standards Card 88, (1995) 2365
[10] M. Pozuelo, S.V. Prikhodko, R. Grantab, H. Zhou, L. Gao, S.D. Sitzman, V. Gambin, V.B. Shenoy, R.F. Hicks, S. Kodambaka, J. Cryst. Growth 312, (2010) 2305
[11] J.H. Kim, P.H. Holloway, Appl. Phys. Lett. 84, (2004) 711
[12] E. Monroy, M. Hermann, E. Sarigiannidou, T. Andreev, P. Hol- liger, S. Monnoye, H. Mank, B. Daudin, M. Eickhoff, J. Appl. Phys. 96, (2004) 3709
[13] J. Johansson, K.A. Dick, P. Caroff, M.E. Messing, J. Bolinsson, K. Deppert, L. Samuelson, J. Phys. Chem. C 114, (2010) 3837
[14] G. Patriarche, F. Glas, M. Tchernycheva, C. Sartel, L. Largeau, J.C. Harmand, G.E. Cirlin, Nano Lett. 8, (2008) 1638
[15] B.M. Shi, M.H. Xie, H.S. Wu, N. Wang, S.Y. Tong, Appl. Phys. Lett. 89, (2006) 151921
[16] C.H. Jia, Y.H. Chen, X.L. Zhou, G.H. Liu, Y. Guo, X.L. Liu, S.Y. Yang, Z.G. Wang, J. Cryst. Growth 312, (2010) 373
[17] Y.L. Wu, L.W. Zhang, G.L. Xie, J. Ni, Y.H. Chen, Solid State Commun. 148, (2008) 247
[18] J. Wu, J. Appl. Phys. 106, (2009) 011101
[19] K.P. Biju, A. Subrahmanyam, M.K. Jain, J. Phys. D, Appl. Phys. 41, (2008) 15540